

Topographic correlations with soil and regolith thickness from shallow-seismic refraction constraints across upland hillslopes in the Valles Caldera, New Mexico

Jared Olyphant,* Jon D. Pelletier and Roy Johnson

Department of Geosciences, University of Arizona, Tucson, AZ, USA

Received 24 February 2015; Revised 2 March 2016; Accepted 9 March 2016

*Correspondence to: Department of Geosciences, University of Arizona, Tucson, AZ, USA. E-mail: jolyphant@email.arizona.edu

ESPL

Earth Surface Processes and Landforms

ABSTRACT: How rock is weathered physically and chemically into transportable material is a fundamental question in critical-zone science. In addition, the distribution of weathered material (soil and intact regolith) across upland landscapes exerts a first-order control on the hydrology of watersheds. In this paper we present the results of six shallow seismic-refraction surveys in the Redondo Mountain region of the Valles Caldera, New Mexico. The P-wave velocities corresponding to soil ($\leq 0.6 \text{ km s}^{-1}$) were inferred from a seventh seismic survey where soil-thickness data were determined by pit excavation. Using multivariable regression, we quantified the relationships among slope gradient, aspect, and topographic wetness index (TWI) on soil and regolith (soil plus intact regolith) thicknesses. Our results show that both soil and regolith thicknesses vary inversely with TWI in all six survey areas while varying directly with slope aspect (i.e. thicker beneath north-facing slopes) and inversely with slope gradient (i.e. thinner beneath steep slopes) in the majority of the survey areas. An empirical model based on power-law relationships between regolith thickness and its correlative variables can fit our inferred thicknesses with R^2 -values up to 0.880 for soil and 0.831 for regolith in areas with significant topographic variations. These results further demonstrate the efficacy of shallow seismic refraction for mapping and determining how soil and regolith variations correlate with topography across upland landscapes. Copyright © 2016 John Wiley & Sons, Ltd.

KEYWORDS: seismic refraction; critical zone; regolith thickness; topographic wetness index; geophysics

Introduction

Soil and regolith thicknesses exert a fundamental control on the hydrologic behavior of watersheds (e.g. Bertoldi *et al.*, 2006; Gochis *et al.*, 2010; Lanni *et al.*, 2013). As such, improving our understanding of and ability to predict soil and regolith thicknesses and how they vary across upland landscapes is a key goal of critical-zone science. Numerous models have been developed that predict the thickness of soil across complex upland (i.e. soil over bedrock) landscapes using high-resolution topographic data as input (e.g. Heimsath *et al.*, 1997; Pelletier and Rasmussen, 2009; Tesfa *et al.*, 2009; Catani *et al.*, 2010; Nicótina *et al.*, 2011; Liu *et al.*, 2013). More recent work has elucidated the controls on the development of the weathered bedrock zone below the soil by topographically induced fracturing (Slim *et al.*, 2014; St Clair *et al.*, 2015), chemical weathering (Lebedeva *et al.*, 2010), and water-table dynamics (Rempe and Dietrich, 2014).

In this paper we use the term soil to refer to the disaggregated/augerable material and intact regolith as the fractured and partially weathered but consolidated/mechanically strong material below the soil and above fractured but

unweathered bedrock (Soil Survey Staff, 1999). Soil depth defined in this way is equivalent to the depth to the paralithic contact. This approach differs somewhat from some geomorphic studies (e.g. Anderson *et al.*, 2013) that define soil only as the unconsolidated material actively being transported down the slope. This transport-related definition of soil leads to thicknesses that are, in some cases, somewhat less than soil depths defined via the depth to the paralithic contact. Defining soil via a transport rather than a strength criterion is appropriate for many scientific questions. However, if the focus of the study is the role of soil in rainfall–runoff partitioning and hydrologic flow paths, it makes sense to define soil via a strength criterion (which tends to vary inversely with porosity and permeability [e.g. Chan, 2006]) rather than a transport criterion.

The goal of this paper is to provide new constraints on the thickness of soil and regolith in Redondo Mountain, New Mexico using seismic-refraction techniques. A key motivation for this work is the fact that isotopic studies have demonstrated systematically higher mean water residence times on north-facing watersheds of Redondo Mountain (Broxton *et al.*, 2009; Zapata-Rios *et al.*, 2015). One hypothesis for this trend is that north-facing watersheds have thicker soils and/or

regolith compared to south-facing watersheds. To test this hypothesis, it is necessary to constrain soil and regolith thicknesses in Redondo Mountain and how they vary as functions of topographic attributes (e.g. slope gradient, aspect, and topographic wetness index [TWI]).

Slope gradient and slope aspect are both recognized controls on the thickness of soil and intact regolith (e.g. Carter and Ciolkosz, 1991; Anderson *et al.*, 2011), but there is no comprehensive process-based understanding of why this is so. Generally, soils and intact regolith are both thinner in steeper landscapes, as erosion rates increase faster than physical weathering, depleting the reservoirs of stored soil and weathered bedrock on the landscape. How slope aspect controls soil and intact regolith thickness is less clear, but likely involves an increase in soil production rates on north-facing slopes due to decreased rates of evapotranspiration and hence greater water availability, at least in water-limited environments such as the south-western United States.

Many previous studies have documented relationships among slope aspect and variations in topography and/or soil thickness in the western United States, but the results defy simple interpretation. Some studies have documented steeper north-facing hillslopes (e.g. Pierce and Colman, 1986; Branson and Shown, 1989; Istanbuluoglu *et al.*, 2008; Poulos *et al.*, 2012; West *et al.*, 2014) while other studies have documented steeper south-facing hillslopes (e.g. Naylor and Gabet, 2007; Burnett *et al.*, 2008; Poulos *et al.*, 2012). Poulos *et al.* (2012) recently developed a method for quantifying hillslope asymmetry at regional-to-continental scales. These authors showed that in the western United States, north- and west-facing hillslopes are steeper, on average, compared with south- and east-facing hillslopes. However, they also documented a shift in hillslope asymmetry in the Idaho Batholith from steeper north-facing hillslopes at elevations below 2000 m above mean sea level (a.m.s.l.) to steeper south-facing hillslopes in areas above 2000 m a.m.s.l. In addition, Poulos *et al.* (2012) observed a shift in the orientation of hillslope asymmetry at latitudes above 49° N, with south-facing hillslopes becoming steeper than north-facing hillslopes above this threshold latitude. This reversal in hillslope asymmetry may be the result of present-day variations in soil production and/or erosion mechanisms with climate variations or of past-glacial activity (Poulos *et al.*, 2012). In this paper we test the hypothesis that soil and regolith are thicker on north-facing slopes (all else being equal) of Redondo Mountain, New Mexico.

In addition, TWI (Beven and Kirkby, 1979), which is a measure of the convergence or divergence of topography, is a proven topographic attribute for characterizing the spatial distribution of zones of surface saturation (Moore *et al.*, 1993) and, therefore, provides a quantitative measure for the relationship between weathering and water availability (Heimsath *et al.*, 1997; Catani *et al.*, 2010; Lebedeva *et al.*, 2010). Although Iverson *et al.* (2004) found that TWI measurements showed stronger correlations with deeper rather than shallower soil moisture measurements, the present-day literature lacks discussion regarding correlation strength between TWI and regolith thickness. However, Rempe and Dietrich (2014) have proposed a quantitative model in which the depth to the water table controls regolith thickness. TWI is inversely related to the depth to the water table (i.e. depth to the water table is generally higher beneath ridgetops and lower beneath valley bottoms while TWI has the opposite trends with topographic position). As such, the Rempe and Dietrich (2014) model suggests that regolith thickness may be a function of TWI, with thicker zones of regolith beneath hillcrests (low TWI) and thinner zones beneath valley bottoms (high TWI).

Shallow seismic refraction acquisition has emerged as an important tool for investigating the structure of soil and regolith. Four recent studies have demonstrated the usefulness of this technique. Befus *et al.* (2011) documented aspect-driven differences in regolith thickness in the Boulder Creek watershed in Colorado. These authors found that north-facing slopes displayed much deeper weathering profiles than their south-facing counterparts. They noted greater moisture retention promoted by denser vegetation cover and longer-lasting snowpacks. They conjectured decreased solar insolation may be the driving force behind this difference in weathering depths. Clarke and Burbank (2011) used multiple short seismic refraction arrays to quantify bedrock-fracture density based on reductions in the seismic velocity of fractured versus intact regolith. More recently, Holbrook *et al.* (2014) and St Clair *et al.* (2015) used seismic refraction and resistivity data to estimate variations in regolith thickness and porosity across four US study sites. Their results show that regolith thickness is greatest on the ridges and thinnest beneath the valley bottoms, ranging from ~40 to 10 m, respectively. In addition, these authors showed, using a rock physics model, that thickness and porosity variations in regolith can be inferred, ultimately allowing the minimum water storage potential of the subsurface to be estimated. Building on these studies, we use shallow seismic refraction results to constrain our proposed model for predicting soil and regolith thicknesses from present-day topography.

Study Area

The Valles Caldera formed ~1.25 Ma in north-central New Mexico, where it is part of the Jemez Mountains Volcanic Field (Goff *et al.*, 2006a). The caldera includes Redondo Mountain (Figure 1), a resurgent dome made up mostly of the Tshirege member of the Bandelier tuff, and many smaller, interior rhyolitic domes that erupted along the caldera ring fracture between ~1.2 Ma and 0.5 Ma (Goff *et al.*, 2006a, 2006b; Phillips *et al.*, 2007).

The modern climate in the Valles Caldera is sub-humid with approximately half of the annual precipitation falling during convective monsoonal storms during the summer months and the other half falling as snow in the winter (Muldavine and Tonne, 2003; Broxton *et al.*, 2009). Average high temperatures at nearby Los Alamos, NM (2231 m above sea level [a.s.l.]) vary from approximately 27 °C in the summer months to 4 °C in the winter months (Muldavine and Tonne, 2003). Average annual precipitation is approximately 46.7 cm at nearby Los Alamos, but it is estimated that this value increases to approximately 90 cm at the rim of the Valles Caldera (Muldavine and Tonne, 2003). The soils within the Valles Caldera range from shallow Andisols, Alfisols, and Inceptisols in the uplands to deep Mollisols in the valleys (Muldavine and Tonne, 2003).

Redondo Mountain is divided into three primary catchments: La Jara, History Grove, and Jaramillo that together cover approximately an area of 10 km² (Figure 1). The Jaramillo catchment has a predominantly northern aspect (58% of total catchment aspect). In contrast, the History Grove and La Jara catchments have predominantly eastern terrain aspects at 59% and 70%, respectively (Zapata-Rios *et al.*, 2015). Conversely to lower elevation catchments in central New Mexico that display greater biomass on north-facing terrains (Gutiérrez-Jurado *et al.*, 2013), the three catchments on Redondo Mountain consists of similar forest coverage with Jaramillo containing the least (72.4%) compared to History Grove (74.9%) and La Jara (81.2%).

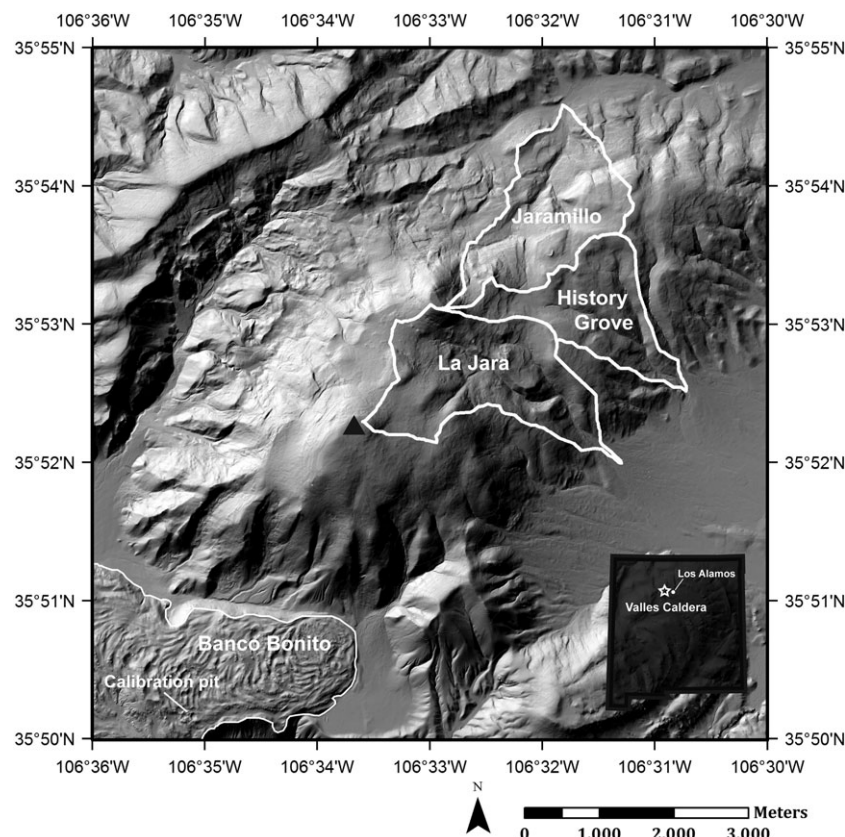


Figure 1. Shaded relief map of the central portion of the Valles Caldera, including Redondo Mountain (black triangle) at c. 1.25 Ma in age and its three prominent watersheds. Outlined in the bottom left is the younger Banco Bonito rhyolite flow (40 ± 5 ka in age), with the location of the explosion pit we used as a calibration site. The inset to the bottom right shows the locations of Los Alamos and the Valles Caldera within northern New Mexico.

Our seismic transects are seven in total, consisting of one upper and one lower profile within each catchment (Figure 2), and one north–south profile within Banco Bonito (Figure 1), a 40 ka rhyolite flow. The Banco Bonito data was used as a calibration for soil thickness because soil thicknesses were previously published for this site by Pelletier *et al.* (2011).

Methods

Seismic data acquisition and processing

We collected seven shallow seismic refraction surveys (six on Redondo Mountain [Figure 2], one on Banco Bonito) from June 5, 2012–June 11, 2012. The data were collected within a single

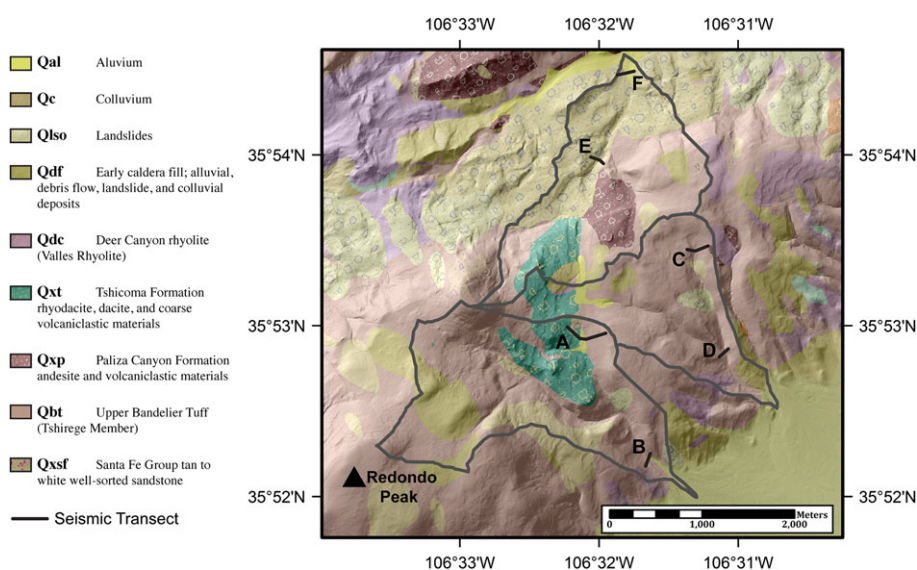


Figure 2. Geologic map from Goff *et al.* (2006a) showing the lithologies in and around Redondo Mountain's La Jara, History Grove, and Jaramillo watersheds. Geologic units on the map are defined in the list to the left. The geologic units are slightly transparent and underlain by shaded relief in order to show topographic expressions. Watershed boundaries are outlined in gray, while seismic transects are labeled with black lines. Lines referred to in the text are upper La Jara (A), lower La Jara (B), upper History Grove (C), lower History Grove (D), upper Jaramillo (E), and lower Jaramillo (F). The peach-colored geologic unit prominent within all three watersheds is the upper Bandelier Tuff (Qbt).

week in order to minimize changes in moisture content. Geophone and source locations were separated by 2.5 m and 12.5 m, respectively (along each survey transect). A Real-Time Kinematic global positioning system (GPS) was used to determine the coordinates and elevations of each source and receiver station. Seismic data were recorded with multiple, linked, 24-channel Geometrics seismographs, typically utilizing 48 to 96 channels connected to 40-Hz single-component geophones. Most often, an 8-kg sledgehammer was used as the impulsive source. Where terrain permitted, we used a 40-kg accelerated weight-drop source to generate seismic impulses by striking a 15 cm × 15 cm × 1.5 cm 10-kg plate. We summed the response of 10 impulses at each source location to improve the signal-to-noise ratio.

Raw data were first loaded into Landmark's SeisSpace® ProMAX® software, where we input survey geometries and manually picked first-break arrivals. Three of our seismic transects (Lines A, C, and E; Figure 2) contained either a sharp bend or gradual curve in their profile orientations in order to follow maximum topographic gradients of their slopes. For this reason, first-break picks from source to receivers, which crossed a significant change in profile orientation, were discarded in order to avoid including data that sampled subsurface materials off the profile. Figure 3 shows an example shot gather and first-break picks from each seismic transect. The data are generally of high quality, providing confidence in our first-break arrival travel time picks. First-arrival times were then input into SeisImager/2D software (OYO/Geometrics, San Jose, CA) and inverted for velocity-depth profiles of the subsurface. Using tomographic inversion, we discretized our starting models, consisting of continuous vertical velocity gradients, into cells of constant velocity 1-m wide and 0.5-m high near

the surface, ultimately increasing to 2-m high at the lowest boundary. For each transect, a total of 28 starting models with minimum velocities spanning 0.25–0.4 km s⁻¹ and maximum velocities spanning 2.0–5.0 km s⁻¹, partitioned into increments of 0.5 km s⁻¹, were computed in order to test the sensitivity of the inversion to the starting model. Ray tracing from each source to receiver produced synthetic travel times. The inversion minimized the L2-norm between observed and predicted data using an iterative non-linear least-squares method for a maximum of 10 iterations. Minimal horizontal smoothing, but no vertical smoothing, was applied during the inversions to combat small-wavelength noise from influencing the final results. Figure 4 shows the observed and predicted first-break travel-time curves for Lines A–F and an example of the ray-tracing coverage and velocity uncertainties for Line D. The ray tracing diagram shows that the inversion resolved only a few ray paths that reached velocities >4.0 km s⁻¹, a consistent result for all of the seismic-refraction profiles in this study. The final inversions resulted in velocity–depth profiles that provide the basis for determinations that are used in further analyses of topographic attributes on soil and regolith thickness discussed later.

Multivariable regression

In order to quantify the role of topography on soil and regolith thicknesses, we performed multivariable regression analyses based on the following empirical model:

$$h(\theta, \alpha, \lambda) = h_0 (\tan \theta)^a (\cos(35 - \alpha) + 1)^b \lambda^c, \quad (1)$$

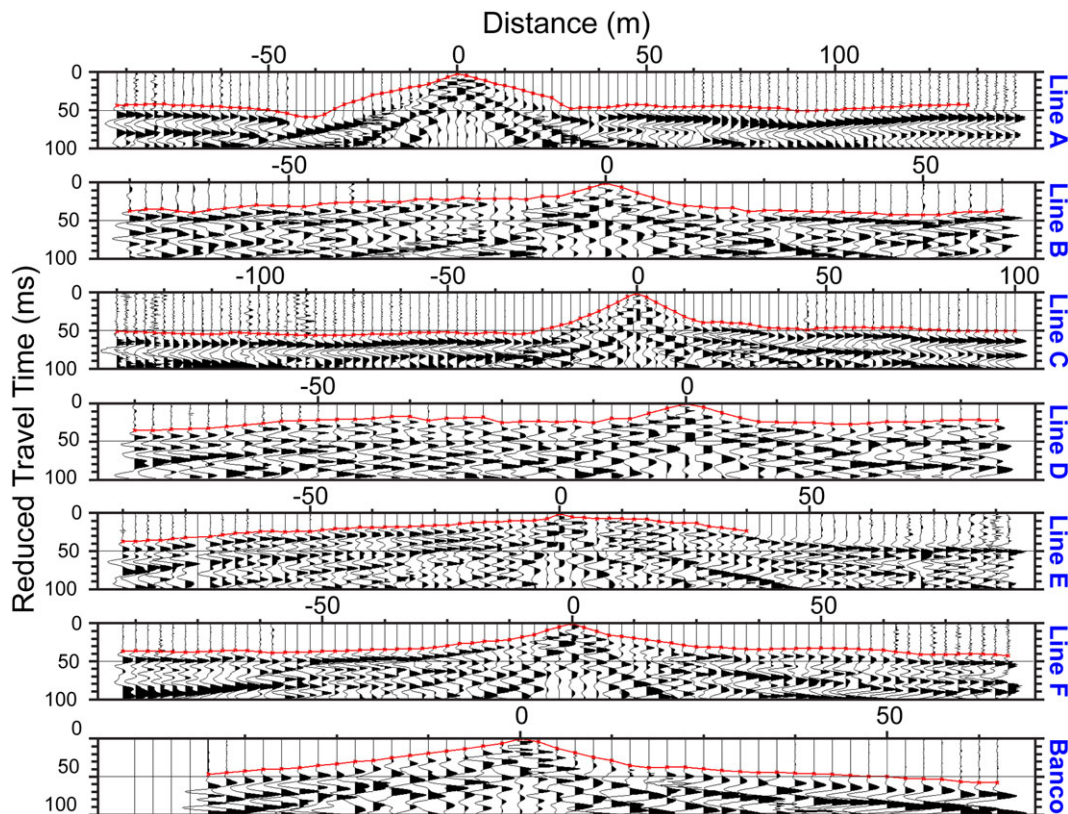


Figure 3. Example shot gathers from each seismic profile in this study. Each display (Lines A–F and Banco) is shown as distance versus reduced travel time (RTT) and clipped at 100 ms in order to focus on the quality of first-break arrivals. The red line of each display connects the manual first-break picks made on each seismic trace. Note the red line terminates at $x = 135.0$ on Line A and $x = 37.5$ on Line E because of shifts in the azimuthal orientations occurring at those locations for the respective lines. RTT velocities were 2.5 km s⁻¹ for Lines A, C, E, F, and Banco, and 4.0 km s⁻¹ for Lines B and D.

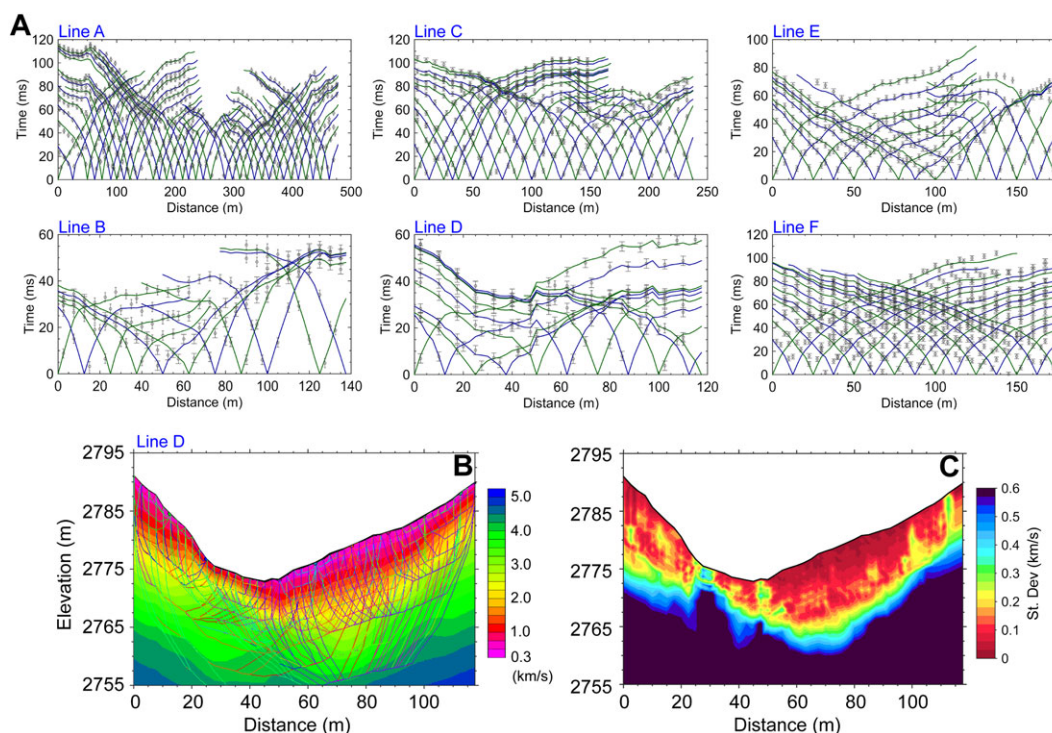


Figure 4. (A) Plots showing the travel-time curves for each transect. The green and blue lines represent the final iterated travel times computed from ray-tracing from each source to receiver through the starting model while the black dots with error bars represent the manually picked first breaks. The plots show the inversion's ability to fit our data well, even at the further offsets where misfit is generally greatest. Note, not all manual picks are shown to maintain clarity. (B) Example result of the ray-tracing algorithm through a starting model with a vertical velocity gradient starting with 0.3 km s^{-1} at the surface and reaching 5.0 km s^{-1} at depth. Notice that very few rays sampled velocities greater than 4.0 km s^{-1} ; a typical result for all of our profiles. Also note that ray coverage diminishes at deeper depths at the ends of the lines. (C) Cross-section of standard deviation in km s^{-1} generated by computing the standard deviation at each point in the subsurface from a suite of 28 inversions with varying starting models. The uncertainty sensibly increases with depth (less constrained), and also is greatest beneath the valley bottom, where the velocity gradient per meter of elevation is greatest. Vertical exaggeration is 2:1.

expressed linearly as:

$$\log(h) = \log(h_0) + \alpha \log(\tan \theta) + b \log(\cos(35 - \alpha) + 1) + c \log \lambda, \quad (2)$$

where h is thickness (in meters), h_0 is the regression intercept, θ is slope (degrees), α is aspect (azimuth), λ is TWI, and a , b , and c are parameters determined by least-squares analysis. We took the tangent of the slope to convert it into slope gradient (m m^{-1}), and also transformed our aspect measurements from degrees to a non-negative scale (using the cosine function and adding 1 in Equations 1 and 2) with limiting values of 2 for N35°E and 0 for S35°W. We analytically determined the 35°-clockwise rotation by averaging the largest R^2 -value over a range of 0° to 60° rotations in increments of one degree computed for each line of our data. Equation 1 is not the only possible mathematical formulation that could describe the relationship among soil/regolith thicknesses and slope gradient, aspect, and TWI, but it has the advantage of being general (i.e. it uses power-law relationships that have the flexibility to characterize linear or non-linear dependencies) and relies on a relatively small number of free parameters.

Slope gradient and aspect measurements coincident with seismic transects were extracted from bare-earth LiDAR-derived 1 m/pixel digital elevation models (DEMs) produced by the National Center for Airborne Laser Mapping (NCALM). The DEMs were smoothed using a $5 \text{ m} \times 5 \text{ m}$ rectangular focal filter prior to computing slope gradient and aspect maps in order to remove small-scale variations in the topography without compromising the shape of the landscape at the hillslope scale. Our TWI values, however, were computed from a $3 \text{ m} \times 3 \text{ m}$

smoothed DEM using the equation:

$$\lambda = \ln\left(\frac{a}{\tan \beta}\right), \quad (3)$$

where a is unit contributing area in meters (i.e. the contributing area divided by the pixel width) determined using the D-infinity algorithm of Tarboton (1997) and β is local slope angle (Beven and Kirkby, 1979). TWI takes on high values in convergence zones (e.g. streams) and low values at divergence zones (e.g. peaks). Additional 5-m smoothing was employed on the TWI maps in order to remove noise at the small scales where pits and mounds associated with tree throw predominate.

One goal of our analyses was to quantify whether any particular topographic variable best explained variations in the underlying soil and regolith thicknesses. Therefore, we normalized our regression coefficients using the Bring (1994) definition:

$$\mathbf{B}_i = \hat{\beta}_i \left(\frac{s_i}{s_y} \right), \quad (4)$$

where \mathbf{B}_i is the normalized regression coefficient, $\hat{\beta}_i$ is the standard regression coefficient, and s_i and s_y are the standard deviations of the independent and dependent variables, respectively. Normalizing our coefficients in this manner puts all our variables in units of standard deviations, removing the effect of variously scaled units among the independent variables. Note that the normalized regression coefficients were used for interpreting our results (relative magnitudes), but not in the predictive modeling (Equation 1) itself.

Calibration for seismic interpretation

In order to interpret our tomographic velocity–depth results in terms of soil thickness, we calibrated them against the measured thicknesses of soil in five pits (i.e. $1\text{ m} \times 2\text{ m}$ areas excavated until refusal using digging bars, augers, and shovels) studied by Pelletier *et al.* (2011). The soil pits were dug within a 120-m-diameter explosion pit (formed by outgassing during the flow event) located in a rhyolitic lava flow adjacent to Redondo Mountain known as Banco Bonito (Figure 1). We surveyed across the explosion pit coincident with the five north-south-trending soil pits. The results in Figure 5 show that the excavated soil-pit depths correlate to a P-wave velocity transition from approximately 0.4 km s^{-1} to 0.6 km s^{-1} . Therefore, we inferred P-wave velocities $\leq 0.6\text{ km s}^{-1}$ to be representative of soil in all our survey sites. Since the study area lies in a protected area, soil pits were not excavated along the other profiles. However, the Banco Bonito pits provide our best analog for soils developing under similar climatic and weathering conditions as the hillslopes on Redondo Mountain. Uncertainties in

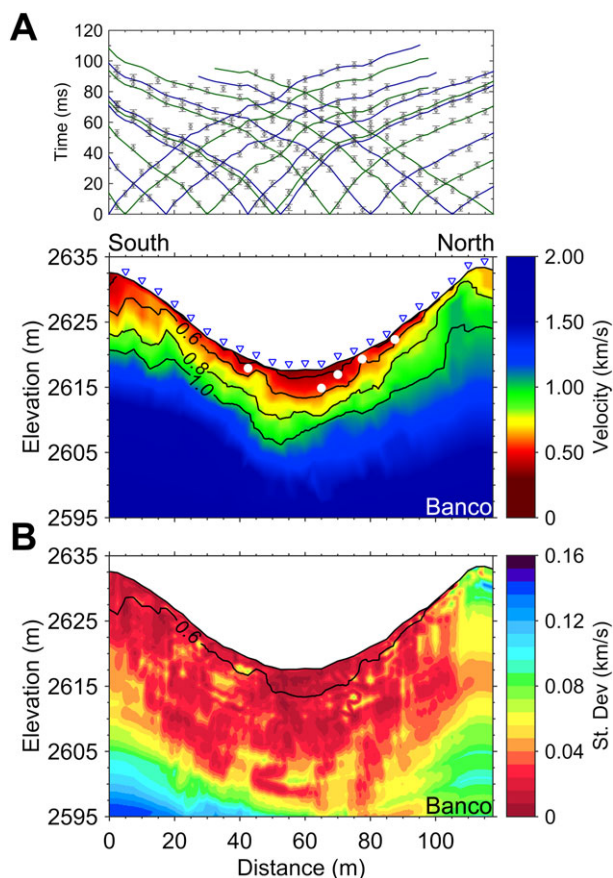


Figure 5. (A) Plot of travel-time curves for the Banco Bonito observed and predicted data. (B) Results of the velocity inversion (top) and standard deviation (bottom) of the Banco Bonito data. The inverted blue triangles depict a subset of the receiver stations. The black contours represent depths of constant velocity, while the white circles show the depths at which soils transition into mechanically stronger intact regolith, as reported in Pelletier *et al.* (2011). All of the white circles terminate at or before the 0.6 km s^{-1} contour, which is therefore the boundary we used for inferring the thickness of soils in this study. The standard deviation results show that the inversion results at the soil velocities are robust for all starting model velocity gradients. The 0.6 km s^{-1} black contour has been superimposed on the standard deviation grid in order to show the uncertainty in the inferred soil boundary (see text for explanation). The depths of the soil pits from left to right are: 1.45, 2.80, 1.90, 1.00, and 1.25 m, respectively. Vertical exaggeration is 2:1.

the soil thicknesses were computed by adding and subtracting the standard deviation of the 0.6 km s^{-1} velocity contour beneath each station and computing the difference in depth (e.g. Figure 5).

At present, no boreholes containing seismic velocity measurements of the bedrock (Bandelier Tuff) spatially coincident with our seismic surveys exist. However, Dey and Kranz (1988) measured density, porosity, P-wave velocity, and S-wave velocity using a core sample from the VC-1 core, drilled within Banco Bonito, that drilled through approximately 100 m of unweathered Bandelier Tuff buried $\sim 200\text{--}300\text{ m}$ below the surface (Table I). The core sample was taken at a depth of 244 m; the sample was later dried and subjected to simulated *in situ* stress conditions, and one vertical directional and two orthogonal (but otherwise unoriented) horizontal directional ultrasonic-velocity measurements were made. These reported P-wave velocity measurements provide some constraints to the basis upon which we interpret the (velocity) transition from intact regolith into the underlying unweathered bedrock. However, because the core sample is measured with ultrasonic frequencies while being subjected to greater confining stresses (at 244 m depth) than the bedrock probed by our exploration seismic frequencies at shallower depths ($< 60\text{ m}$), the core sample is not a direct measurement of the Bandelier Tuff probed by our seismic surveys. Thus, we analyzed velocity–depth profiles beneath receiver stations along our transects, and used the Dey and Kranz (1988) velocity measurements as a range (i.e. $2.54\text{--}4.12\text{ km s}^{-1}$) within which we can expect the transition into unweathered bedrock to occur. In particular, we postulate that the depths where the velocity gradient is steepest (within $2.54\text{--}4.12\text{ km s}^{-1}$) represents the transition into more consolidated, less weathered rock. The top of Figure 6 shows a suite of velocity–depth profiles that span the length of Line A. Within each profile, we marked the depth of the onset of the steepest velocity gradient between 2 and 4 km s^{-1} . In addition, the bottom of Figure 6 shows the onset depth every 12.5 m across the entire transect. We noted that most of the strong breaks occurred between 2.54 km s^{-1} and 3.37 km s^{-1} . With this result being consistent across all of our lines (Lines A–F), we inferred that the transition from the base of the intact regolith into unweathered bedrock occurs at the depth of the 2.95 km s^{-1} (i.e. the average of 2.54 and 3.37) velocity contour (solid-black line, Figure 6) plus or minus the difference in depths associated with the 2.54 km s^{-1} and 3.37 km s^{-1} velocity contours (dashed-black lines, Figure 6). As a result of this analysis, we posit that the 4.12 km s^{-1} velocity reported in Dey and Kranz (1988) was measured along a particularly fast direction using standard ultrasonic frequencies in a standard, very small sample taken at $\sim 200\text{ m}$ depth greater than the bedrock probed in our surveys. Our seismic results, which were obtained with several different orientations with respect to the tuff unit, do not show large variations in velocity and do not indicate a distinct directional dependence for faster or slower velocities. Even so, if we include the 4.12 km s^{-1} velocity in our averaged velocity, we get a value of 3.34 km s^{-1} , which, while only indicating a minor increase in our regolith thickness values, still falls within the range of our error bars.

Table I. Bandelier Tuff elastic properties.

Depth (m)	Density (g cm^{-3})	Porosity (%)	V_p^a (km s^{-1})	V_s^a (km s^{-1})
244	1.75	24.5	2.54:3.37:4.12	1.53:1.92:2.18

^aValues represent measurements made in the vertical directions: first horizontal: second horizontal direction. Table modified from Dey and Kranz (1988).

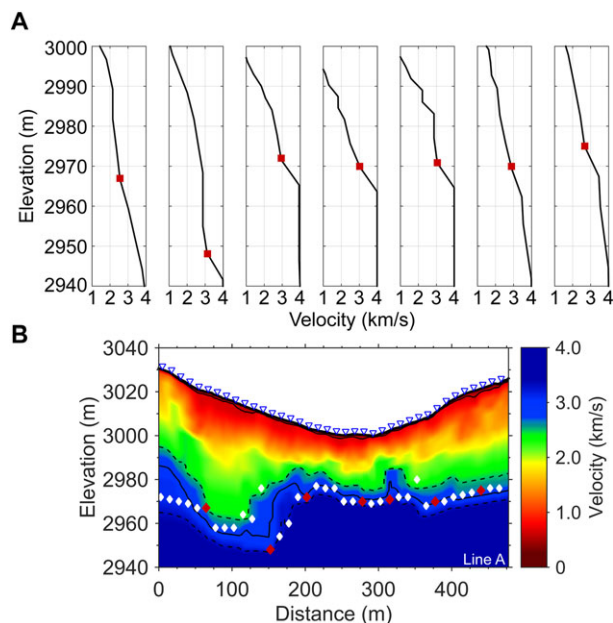


Figure 6. (A) Velocity-depth profiles beneath seven stations across Line A at offsets of $x=65.0, 152.5, 202.5, 277.5, 315.0, 377.5$, and 440.0 m. The red squares mark the onset of steepest velocity gradient between 2.5 and 4.0 km s^{-1} , i.e. the inferred transition from intact regolith into unweathered bedrock. Notice that most of the onsets occur near a velocity of 3.0 km s^{-1} . (B) Onset depths picked from profiles shown in (A) as red diamonds, as well as white diamonds from profiles not shown. The onset depths generally fall within the dashed 2.54 and 3.37 km s^{-1} velocity contours.

Results

Seismic tomography

Figure 7A (top) shows the velocity inversion and standard deviation (bottom) depth sections for upper La Jara (Line A). The upper La Jara drainage represents the broadest valley within our study and is located near the headwaters of the drainage basin. The profile transitions from Bandelier Tuff into the Tshicoma Formation at the valley bottom; however, we do not see a notable change in subsurface velocity across the geologic contact. Thus, it is difficult to unequivocally interpret this transition based on the tomographic-velocity results alone. Therefore, in the absence of complementary geophysical data (e.g. gravity and/or magnetic), and measured sonic or empirical velocities of the Tshicoma Formation, we maintain our interpretation of the transition from unweathered into weathered bedrock (see earlier) to report inferred regolith thicknesses across the profile. The resulting regolith thicknesses average approximately 49 ± 10 m for the southwest-facing slope and 42 ± 6 m for the northeast-facing slope, with 27 ± 4 m beneath the valley bottom. These values appear high compared to other studies based on crystalline bedrock (Holbrook *et al.*, 2014; St Clair *et al.*, 2015); however, this region of Redondo Mountain is strongly faulted and therefore likely highly fractured, potentially resulting in greater weathering and slower seismic velocities at depth. Soil thicknesses are uniformly thin across the entire transect, averaging 1 ± 1 m.

The inversion results for the lower La Jara profile (Figure 7B, top) are a product of a shorter (117.5 m), straight (22° , north-northeast–south-southwest [NNE–SSW]) survey that consists only of Upper Bandelier Tuff parent material and is located near the terminus of the watershed. The inversion shows 3 ± 1 m and 2 ± 1 m mean thickness soils for the northeast- and southwest-facing slopes, respectively, with soils

that thin to values beneath 1 m in the valley bottom. Similarly, mean regolith thicknesses are 17 ± 2 m and 10 ± 2 m for the northeast- and southwest-facing slopes, respectively, and 8 ± 2 m beneath the valley bottom.

The History Grove inversion results represent another pair of transects surveyed across a south-facing drainage. However, this drainage is narrower and steeper than the La Jara drainage and the parent material beneath the transects is characterized solely by upper Bandelier Tuff. The upper History Grove profile (Figure 8A) contains a prominent thick weathering profile, with mean soil thicknesses of 6 ± 2 m and 7 ± 2 m for the southeast- and southwest-facing slopes, respectively, and 5 ± 1 m beneath

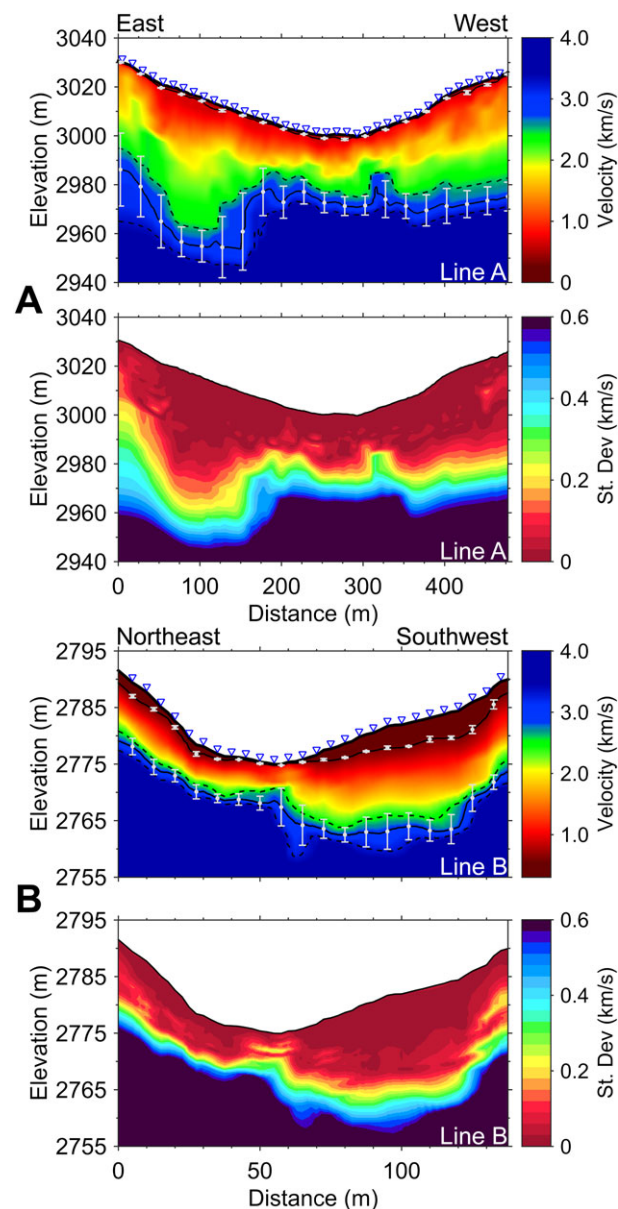


Figure 7. (A) Velocity-depth result of the inversion (top) for Line A (upper La Jara) and its standard deviation (bottom). The solid black contour just beneath the topography shows the soil thickness (i.e. 0.6 km s^{-1} contour) with white error bars showing the uncertainty at intervals of every 10th station. The solid black contour at depth depicts the mean regolith thickness as inferred by the 2.95 km s^{-1} velocity contour. The dashed lines above and below are the minimum (2.5 km s^{-1}) and maximum (3.4 km s^{-1}) contours, respectively, from which the white error bars were determined. The inverted blue triangles show a subset of the receiver stations. Vertical exaggeration is 3:1. (B) An identical display, however for the Line B (lower La Jara) results with error bars plotted every third station. Vertical exaggeration is 2:1.

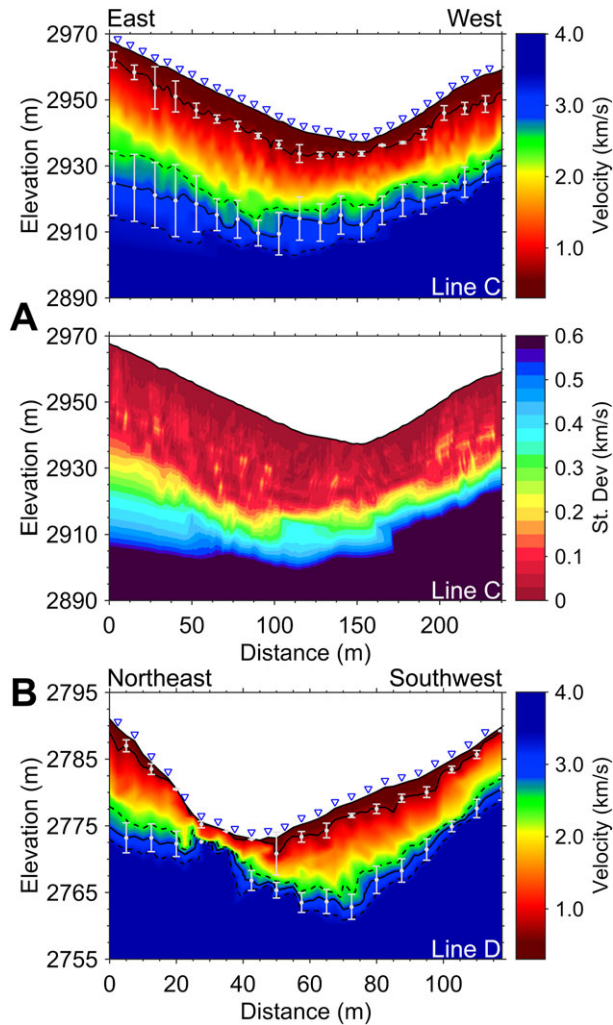


Figure 8. (A) Velocity-depth result of the inversion (top) for Line C (upper History Grove) and its standard deviation (bottom). The solid black contour beneath the topography shows the soil thickness with white error bars showing the uncertainty at intervals of every fifth station. The solid black contour at depth depicts the mean regolith thickness as inferred by the 2.95 km s^{-1} velocity contour. The dashed lines above and below are the minimum (2.5 km s^{-1}) and maximum (3.4 km s^{-1}) contours, respectively, from which the white error bars were determined. The inverted blue triangles show a subset of the receiver stations. Vertical exaggeration is 2:1. (B) Velocity-depth result of the inversion for Line D (lower History Grove) with error bars plotted every third station. The accompanying standard deviation plot is shown in Figure 4C. Vertical exaggeration is 2:1.

the valley bottom. Regolith thicknesses display greater relative differences, with mean thicknesses of $27 \pm 4 \text{ m}$ and $37 \pm 7 \text{ m}$ for the southeast- and southwest-facing slopes, respectively, and $25 \pm 6 \text{ m}$ beneath the valley bottom.

Inversion results for the lower History Grove profile (Figure 8 B) are characterized by steep velocity gradients beneath the southwest-facing slope and valley bottom. At the surface, loose angular rocks form a scree slope, consistent with the near zero soil thickness at that location ($18.0 \leq x \leq 27.5$; Figure 8B). Mean soil thicknesses are $2 \pm 1 \text{ m}$ and $1 \pm 1 \text{ m}$ for the northeast- and southwest-facing slopes, respectively, and less than a meter beneath the valley bottom. Meanwhile, mean regolith thicknesses are $12 \pm 2 \text{ m}$ and $11 \pm 2 \text{ m}$ for the northeast- and southwest-facing slopes, respectively, and $5 \pm 1 \text{ m}$ beneath the valley bottom.

Results for the upper Jaramillo profile, characterized by an area overlain entirely by Quaternary landslide deposits, are shown in Figure 9A. The results suggest the landslide deposits

make little difference in the soil and regolith thicknesses relative to the other profiles in this study. Specifically, the mean soil thicknesses for the northwest- and southeast-facing slopes are $5 \pm 1 \text{ m}$ and $1 \pm 1 \text{ m}$, respectively, while mean regolith thicknesses are $27 \pm 9 \text{ m}$ and $34 \pm 5 \text{ m}$, respectively, and $24 \pm 6 \text{ m}$ beneath the valley bottom. Thus, we interpret that the landslide deposits do not extend indefinitely with depth, and when the velocities reach values of 2.5 km s^{-1} and greater, it suggests a transition to underlying unweathered Bandelier Tuff.

Inversion results for the lower Jaramillo profile (Figure 9B) represent the lowest elevation survey (excluding Banco Bonito) completed in this study. Significant low vertical velocity gradients resolved in the inversion resulted in large uncertainties (error bars; Figure 9B) at depth. Mean regolith thicknesses are $42 \pm 8 \text{ m}$ for the east-facing hill and $36 \pm 10 \text{ m}$ for the west-facing hill, and $36 \pm 6 \text{ m}$ beneath the valley bottom. Mean soil thicknesses are thin throughout, resulting in $1 \pm 1 \text{ m}$ across the entire transect.

Regression analyses

Standard multivariable regression results for soil and regolith thicknesses are presented in Table II. The results were computed from slope gradient, slope aspect, TWI, and soil/regolith thickness beneath each station. Soil and regolith thicknesses beneath each station were computed using the methods discussed earlier. Overall, the soil regression results (Table II) indicate a negative correlation between soil thickness and slope gradient (i.e. steeper topography has thinner soils) for four of six profiles, while five of six profiles showed a positive correlation between thickness and slope aspect (i.e. north-facing slopes have thicker soils). All six profiles show a strong negative correlation with TWI, unequivocally stating that soils are thinnest in the valley bottoms where water is converging. The R^2 -values are variable amongst profiles, spanning 0.269–0.880, with an average of 0.467. The normalized soil regression coefficients show TWI as the dominant control, followed by slope gradient and, lastly, slope aspect.

The regolith regression results shown in Table II show that two of six profiles contain a negative correlation between regolith thickness and slope gradient, while four of six profiles show a positive correlation with slope aspect, and again all six profiles display a negative correlation with TWI. The R^2 -values are higher than for the soils, ranging from 0.406 to 0.831 with an average of 0.511. The normalized regolith coefficients show that TWI and aspect have the largest correlation with regolith thickness. Figure 10 shows each of the six Redondo Mountain cross-sections with seismically picked soil and regolith thicknesses as well as their predicted depths determined from regression analysis. The plots make it evident that the model is incapable of predicting short-wavelength variations in thickness (e.g. regolith thickness decrease between distances 20 m and 40 m along Line D). However, the primary goal is to predict mean soil or regolith thicknesses for which small-wavelength variations are relatively secondary; the model is capable of consistently predicting thicker soils for less-steep surfaces and thicker weathered bedrock/regolith thicknesses for areas with a low TWI and northerly-facing topography.

In order to make landscape-scale predictions of soil and regolith thickness across the entire Redondo Mountain region, we aggregated all of our data and performed the same regression analysis. The resulting coefficients (Equation 1) for regolith are $h_0 = 4.748$, $a(\text{slope}) = -0.638$, $b(\text{aspect}) = 0.027$, and $c(\text{TWI}) = -1.333$. Figure 11A shows the

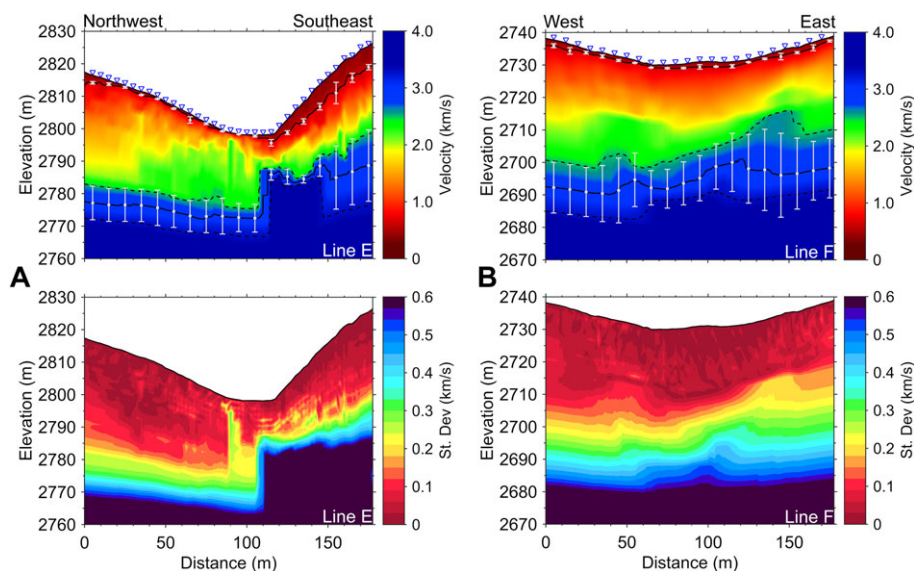


Figure 9. (A) Velocity-depth result of the inversion (top) for Line E (upper Jaramillo) and its standard deviation (bottom). The solid black contour beneath the topography shows the soil thickness with white error bars showing the uncertainty at intervals of every fourth station. The solid black contour at depth depicts the mean regolith thickness as inferred by the 2.95 km s^{-1} velocity contour. The dashed lines above and below are the minimum (2.5 km s^{-1}) and maximum (3.4 km s^{-1}) contours, respectively, from which the white error bars were determined. The inverted blue triangles show a subset of the receiver stations. Note the sharp horizontal change in velocities at $x \approx 110 \text{ m}$. This is an imaging artifact from having a sharp kink in the line at the base of the valley. Vertical exaggeration is 2:1. (B) An identical display, however for the Line F (lower Jaramillo) results with error bars plotted every fourth station. Vertical exaggeration is 2:1.

resulting regolith thickness map. In addition, a map of uncertainty in thickness (Figure 11B) was also computed using regression coefficients determined from the minimum and maximum thicknesses as described earlier. Note that results along the tops of peaks, such as Redondo Peak, should not be considered reliable since none of our transects traversed hillcrests. Nevertheless, the predicted values along hillslopes and beneath valley bottoms provide the most reliable estimate of regolith thicknesses in the region to date.

Aggregated coefficients for soil thickness were also computed; however, the resulting coefficients failed to explain more than $\sim 20\%$ of the variation in thickness. In addition, the results showed a positive correlation with slope, suggesting soil thickness is greatest beneath steep slopes. This is fundamentally incorrect (e.g. Figures 7B and 8B), and instead is the result of including the inferred thin soils beneath the valley bottoms in the analysis. Thin soils beneath valley bottoms suggest that thin soils correlate with shallow slope gradients. There is no

Table II. Regression results for soil and regolith.

	La Jara (upper)	La Jara (lower)	History Grove (upper)	History Grove (lower)	Jaramillo (upper)	Jaramillo (lower)
<i>Soils</i>						
<i>Standard coefficients</i>						
h_0	0.927	3.612	3.665	1.602	7.598	2.229
a (slope)	-0.373	0.478	0.053	-0.565	-0.315	-0.103
b (aspect)	0.020	0.246	-0.122	0.027	0.226	0.010
c (TWI)	-0.771	-1.195	-1.152	-0.973	-3.973	-1.188
R^2	0.349	0.607	0.399	0.269	0.880	0.295
<i>Normalized coefficients</i>						
a (slope)	-0.472	0.370	0.045	-0.505	-0.270	-0.215
b (aspect)	0.154	0.653	-0.768	0.238	0.038	0.016
c (TWI)	-0.516	-0.385	-0.773	-0.544	-1.176	-0.653
<i>Regolith</i>						
<i>Standard coefficients</i>						
h_0	6.040	4.598	4.429	4.885	4.373	4.360
a (slope)	0.123	0.302	0.333	-0.551	-0.395	0.060
b (aspect)	0.039	0.196	-0.091	0.041	-1.625	0.156
c (TWI)	-1.073	-0.868	-0.397	-1.774	-0.567	-0.335
R^2	0.549	0.831	0.408	0.434	0.406	0.438
<i>Normalized coefficients</i>						
a (slope)	0.127	0.373	0.413	-0.430	-0.994	0.268
b (aspect)	0.241	0.829	-0.826	0.309	-0.806	0.535
c (TWI)	-0.586	-0.445	-0.385	-0.866	-0.492	-0.390

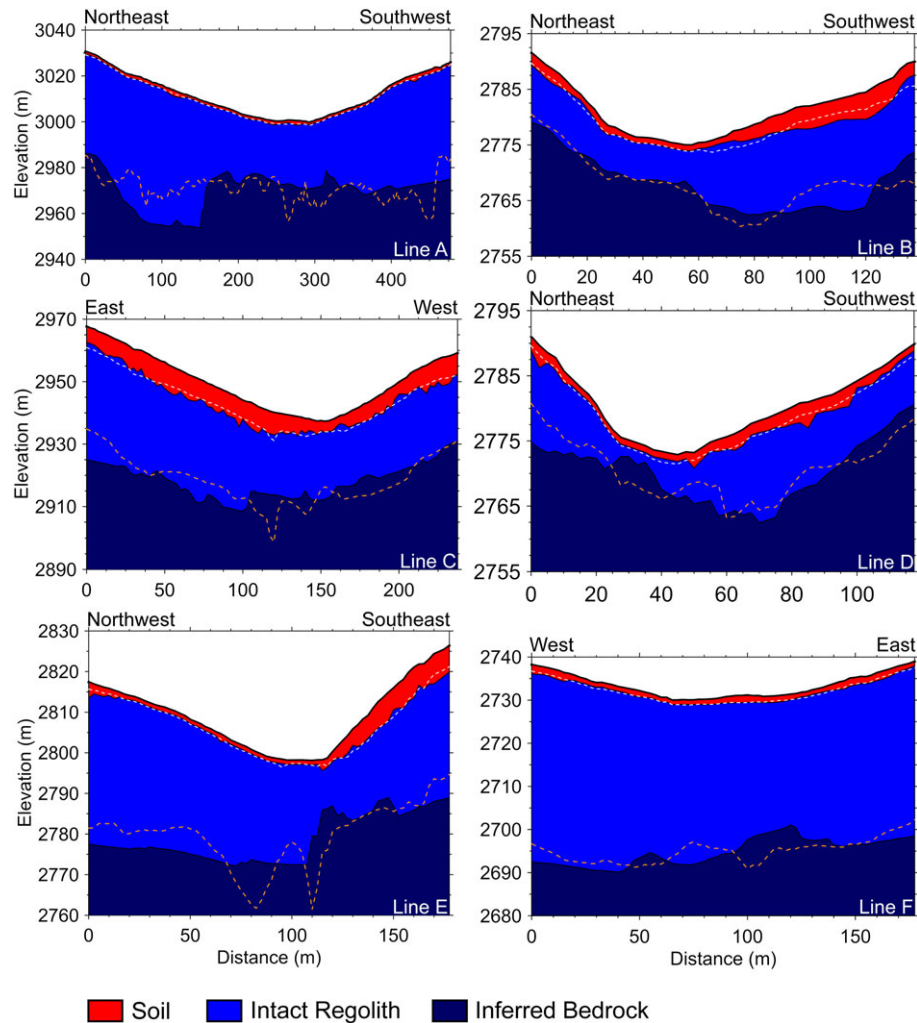


Figure 10. Cross-sections depicting inferred soil and intact regolith thicknesses (red and blue polygons) overlying inferred bedrock (purple polygons). In addition, the predicted depths to the base of soil and regolith using our regression results and empirical model are shown as dotted white and orange lines, respectively. Polygon boundaries were picked from the inversion results shown previously. All cross-sections are displayed at 2:1 vertical exaggeration except Line A, which is 3:1.

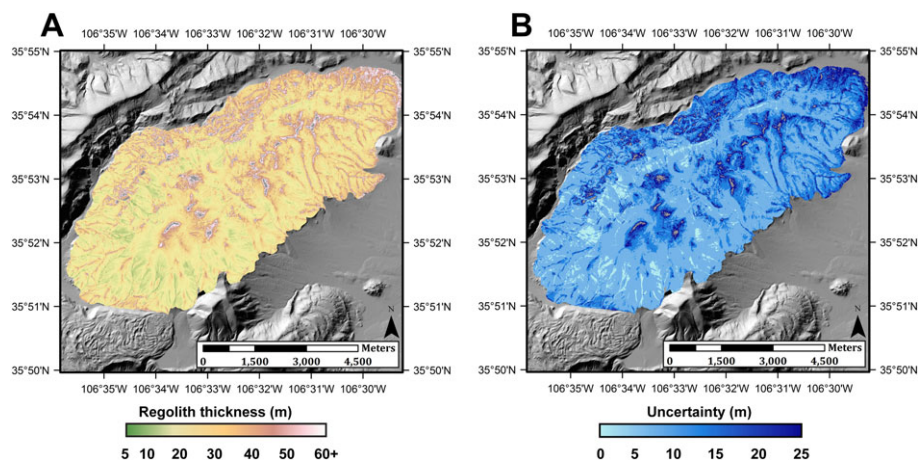


Figure 11. (A) Map of predicted regolith thickness generated using regression coefficients computed from the aggregation of all our data. The background is the shaded relief map shown in Figure 1. Red and white shades represent thicker regolith, typically shown beneath ridgetops, while yellow and green shades represent thinner regolith, typically beneath hillslopes and the valley bottoms. In the absence of steep slopes, the values are dominantly controlled by a negative correlation with topographic wetness index (TWI) and a positive correlation with slope aspect. In areas with steep topography, slope gradient becomes a more important factor (e.g. the steeper south-facing drainages). The thickness values at ridgetops are poorly constrained with our dataset, therefore the white shades should be interpreted cautiously. (B) Complementary map showing uncertainty (in meters) of regolith thickness. The results were generated by subtracting a minimum regolith thickness map from a maximum regolith thickness map computed via minimum and maximum thickness regression coefficients. In general, our regolith thickness values have up to a ~25% uncertainty at any specific location. In both maps, the gray shades at the tops of peaks represent areas where thickness calculations were not performed due to our topographic attributes converging to zero, causing instabilities in the model.

distinction between hillslopes and valley bottoms in the empirical model. We tested this hypothesis by incorporating the curvature of the landscape in order to remove soil thickness data beneath valley bottoms (i.e. removed stations with small slope gradients and negative curvature). Removal of ~35% of our data was required in order to resolve a negative correlation between slope gradient and soil thickness. For this reason, we defer the prediction of soil thicknesses at the landscape scale for another study that either removes valley bottoms entirely, or employs a model capable of accounting for the different processes of soil development occurring beneath hillslopes and valley bottoms.

Discussion

Our study of six transects across upper and lower sections of three different drainages illuminates the variability in soil and regolith thicknesses throughout a mountainous landscape. The seismic profile locations and their orientations were chosen in order to image the hillslopes along the direction of maximum slope gradient, i.e. along transects parallel to soil–water transport where soil and regolith thickness can be expected to vary most. This approach is geomorphically robust; the advantage is that the transect can resolve the subsurface architecture of the hillslope along the direction of maximum weathering and erosion. The disadvantage to this approach is that arrivals recorded across the drainages have bottoming points which may lie off the transect. Restricting such arrivals tends to reduce the depth of resolution near the valley bottoms. For our data, this issue was most significant for the inversion of Line E, where the bend in the profile was sharp (~30°) and the valley bottom was narrow. For Lines A and C, however, the bends were not as abrupt and the valley bottoms were not as narrow. For this reason, we were able to include more of the first-break picks closer to the transect bends. In all cases, no data from stations for which a straight-line path from source to receiver deviated more than 2.5 m (one station interval) from the azimuth of the transect were used in the inversions. Recently published work that imaged regolith thickness variations across hillslopes and valley bottoms in other regions showed that regolith thickness decreases beneath valley bottoms, often to ~10 m (Holbrook *et al.*, 2014; St Clair *et al.*, 2015). Our ray paths sampled to depths of at least 10 m (or more) near the profile bends, suggesting that our restricted ray paths beneath the valley bottoms were adequate to reasonably constrain regolith thicknesses in the valley bottoms.

Our soil-regression results complement previous process-based geomorphic models (Heimsath *et al.*, 1997; Pelletier and Rasmussen, 2009) that indicate soil thicknesses are dominantly controlled by their inverse correlation with hillslope curvature (i.e. steeper slopes have thinner soils). We tested the addition of curvature to our model, but it did not provide an additional predictive advantage beyond TWI. In addition, we tested the substitution of curvature for TWI and found a decrease in the ability of the model to fit our soil and regolith thicknesses. For these reasons, we did not include curvature as a predictive parameter. Our results show a negative correlation between TWI and inferred soil thicknesses, which suggests that soil thicknesses decrease beneath valley bottoms and increase beneath hilltops. This is not consistent with process-based models, and is a consequence of our inferred soil thicknesses consistently decreasing beneath valley bottoms. The decreases in soil thicknesses beneath valley bottoms may indeed be a correct result; however, the soil thicknesses are inferred from seismic velocities that are subject to the potential effects of water saturation within the lowest

parts of the valleys. Saturation of pore spaces with water will increase the propagation velocities of seismic waves traveling through soils to velocities above 0.6 km s^{-1} , generally resulting in diminished inferred soil thicknesses. Thus, complementary *in situ* resistivity data is recommended in order to support soil thickness measurements beneath valley bottoms. Along the hillslopes, however, water saturation is less of a factor because the soils tend to drain under the influence of gravity. Our hillslope results show that inferred soil thicknesses exhibit a negative correlation with slope gradient and a positive correlation with slope aspect. The slope aspect results support the hypothesis that north-facing hillslopes are characterized by relatively thicker soils within the same drainage due to decreased solar insolation; however, we did not find thicker soils throughout the north-facing (Jaramillo) watershed relative to the south-facing History Grove and La Jara watersheds. Generally, soil thicknesses on the northwest-facing slope of the upper Jaramillo profile (Line E) are comparable to the thickest soils inferred in this study (i.e. ~5 m).

Our regolith regression results (Table II) show generally positive correlations with slope gradient and the cosine of slope aspect and negative correlations with TWI. The aspect results are similar to the results of Befus *et al.* (2011), who found consistently thicker regolith on north-facing slopes. One possible reason for the negative correlation between regolith thickness and TWI is that regolith thickness is controlled, in part, by the depth to the permanent water table as proposed by Rempe and Dietrich (2014). In the Rempe and Dietrich (2014) model, regolith develops only in the unsaturated zone, which is thicker beneath ridgetops and thinner beneath valley bottoms (where the water table is assumed to intersect the surface). Streams draining Redondo Mountain are gaining streams where springs are common, hence the assumption that the water table intersects the topography at the valley bottom is a good approximation for our study sites. In the Rempe and Dietrich (2014) model the precise thickness of the unsaturated zone depends on the rate of channel downcutting, the porosity, and the bedrock hydraulic conductivity, but in all cases the regolith is deep under ridgetops and shallow under valley bottoms. Regolith thickness values commonly show this association with topographic position (e.g. Pavich *et al.*, 1989; Brantley and White, 2009; Lebedeva and Brantley, 2013). TWI values have the opposite relationship to topographic position, i.e. values are small near ridgetops where contributing area goes to zero, and high near valley bottoms where contributing area is large. As such, our finding that regolith tends to be relatively thin beneath valley bottoms and thicker on side slopes and near ridgetops is consistent with the predictions of the Rempe and Dietrich (2014) model.

Conclusions

In this study, we surveyed six shallow seismic refraction profiles (with a seventh for calibration) in order to image soil and regolith thicknesses and improve our understanding of the subsurface in the temperate upland landscape of Valles Caldera. In order to differentiate between soil, intact regolith (weathered bedrock), and unweathered bedrock from seismic velocity measurements, we used depths calibrated from excavated soil pits and published core velocity data from the area. We combined inferred soil and regolith thicknesses from the seismic results with slope-gradient, slope-aspect, and TWI calculations derived from $1 \text{ m} \times 1 \text{ m}$ bare-earth LiDAR data to analyze the influence of topography on subsurface weathering-profile thicknesses using multivariable regression modeling. Our results indicate that soil thicknesses (generally

<3 m) are more sensitive to TWI and slope aspect rather than slope gradient in the absence of steep slopes. However, we conclude that additional geophysical data and borehole data within the valley bottoms, as well as a more refined predictive model capable of distinguishing between the valley bottoms and hillslopes, are desirable to more comprehensively and accurately constrain soil thickness variations across upland landscapes.

For regolith thickness, our results show TWI to be the key predictive topographic attribute, followed in suite by slope aspect and gradient. We conclude that robust first-order approximations of regolith thickness variations in upland landscapes are well-suited for our empirical model. Ultimately, with three topographic attributes, we were able to fit our inferred soil and regolith thicknesses with average R^2 -coefficients of 0.436 and 0.511, respectively, for all lines. We aggregated our data and produced regression coefficients for regolith thickness that accurately model the broad-scale variations based on topography.

Generally, our results show that shallow seismic-refraction methods are capable of providing robust soil and regolith thickness data for input into topographic models, from which predictions of soil and regolith thicknesses elsewhere can be extrapolated. In addition, these predictions may provide constraints for other geomorphological and hydrological studies within the Jemez Critical Zone.

Acknowledgements—The authors thank Scott Compton, Saba Keynejad, Noah McDougall, and Xavier Zapata-Rios for assistance in the field. The authors also thank Kiriaki Xiluri for computer support and James Broermann for his helpful discussions and insights throughout. The authors also thank Steven Holbrook and Matt Jungers for their insightful reviews, which helped them to make important improvements to this manuscript. Instruments used in the field were provided by the PASSCAL facility of the Incorporated Research Institutions for Seismology (IRIS) through the PASSCAL Instrument Center at New Mexico Tech. The authors thank Greg Chavez (PASSCAL) for providing computers and software used in some of the post-experiment processing. Initial seismic processing software used in this research was provided by Halliburton Energy Advancement, Inc. via the Landmark University Grant Program; inversions were computed with software provided by Geometrics, Inc. This study was funded by the National Science Foundation (EAR-0724958 and EAR-1331408).

References

- Anderson RS, Anderson SP, Tucker GE. 2013. Rock damage and regolith transport by frost: an example of climate modulation of the geomorphology of the critical zone. *Earth Surface Processes and Landforms* **38**: 299–316. DOI:10.1002/esp.3330.
- Anderson SP, Anderson RS, Hinckley E-LS, Kelly P, Blum A. 2011. Exploring weathering and regolith transport controls on Critical Zone development with models and natural experiments. *Applied Geochemistry* **26**(Supplement): S3–S5. DOI:10.1016/j.apgeochem.2011.03.014.
- Befus KM, Sheehan AF, Leopold M, Anderson SP, Anderson RS. 2011. Seismic constraints on critical zone architecture, Boulder Creek Watershed, Colorado. *Vadose Zone Journal* **10**: 915–927. DOI:10.2136/vzj2010.0108.
- Bertoldi G, Rigon R, Over TM. 2006. Impact of watershed geomorphic characteristics on the energy and water budgets. *Journal of Hydrometeorology* **7**: 389–403. DOI:10.1175/JHM500.1.
- Beven KJ, Kirkby MJ. 1979. A physically based, variable contributing area model of basin hydrology [Un modèle à base physique de zone d'appel variable de l'hydrologie du bassin versant]. *Hydrological Sciences Bulletin* **24**: 43–69. DOI:10.1080/02626667909491834.
- Branson FA, Shown LM. 1989. *Contrasts of Vegetation, Soils, Microclimates, and Geomorphic Processes between North- and South-facing Slopes on Green Mountain near Denver, Colorado*, USGS Water-resources Investigation Report 89–4094. US Geological Survey: Reston, VA.
- Brantley SL, White AF. 2009. Approaches to modeling weathered regolith. *Reviews in Mineralogy and Geochemistry* **70**: 435–484. DOI:10.2138/rmg.2009.70.10.
- Bring J. 1994. How to standardize regression coefficients. *The American Statistician* **48**: 209–213. DOI:10.1080/00031305.1994.10476059.
- Broxton PD, Troch PA, Lyon SW. 2009. On the role of aspect to quantify water transit times in small mountainous catchments. *Water Resources Research* **45**. DOI:10.1029/2008WR007438.W08427.
- Burnett BN, Meyer GA, McFadden LD. 2008. Aspect-related microclimatic influences on slope forms and processes, northeastern Arizona. *Journal of Geophysical Research: Earth Surface* **113**. DOI:10.1029/2007JF000789.F03002.
- Carter BJ, Ciolkosz EJ. 1991. Slope gradient and aspect effects on soils developed from sandstone in Pennsylvania. *Geoderma* **49**: 199–213. DOI:10.1016/0016-7061(91)90076-6.
- Catani F, Segoni S, Falorni G. 2010. An empirical geomorphology-based approach to the spatial prediction of soil thickness at catchment scale. *Water Resources Research* **46**. DOI:10.1029/2008WR007450.W05508.
- Chan KY. 2006. Bulk density. In *Encyclopedia of Soil Science, volume 1*, Lal R (ed). Taylor & Francis: London; 191–193.
- Clarke BA, Burbank DW. 2011. Quantifying bedrock-fracture patterns within the shallow subsurface: implications for rock mass strength, bedrock landslides, and erodibility. *Journal of Geophysical Research: Earth Surface* **116**. DOI:10.1029/2011JF001987.F04009.
- Dey TN, Kranz RL. 1988. State of stress and relationship of mechanical properties to hydrothermal alteration at Valles Caldera core hole 1, New Mexico. *Journal of Geophysical Research: Solid Earth* **93**: 6108–6112. DOI:10.1029/JB093iB06p06108.
- Gochis DJ, Vivoni ER, Watts CJ. 2010. The impact of soil depth on land surface energy and water fluxes in the North American Monsoon region. *Journal of Arid Environments* **74**: 564–571. DOI:10.1016/j.jaridenv.2009.11.002.
- Goff F, Gardner JN, Reneau SL, Goff CJ. 2006a. *Preliminary Geologic Map of the Redondo Peak Quadrangle, Sandoval County, New Mexico*, New Mexico Bureau of Geology and Mineral Resources Open-File Digital Geologic Map OF-GM 111. New Mexico Bureau of Geology and Mineral Resources: Socorro, NM.
- Goff F, Reneau SL, Goff CJ, Gardner JN, Drakos PG, Katzman D. 2006b. *Preliminary Geologic Map of the Valle San Antonio Quadrangle, Sandoval County, New Mexico*. In New Mexico Bureau of Geology and Mineral Resources Open-File Digital Geologic Map OF-GM 132. Socorro, NM: New Mexico Bureau of Geology and Mineral Resources.
- Gutiérrez-Jurado HA, Vivoni ER, Cikloski C, Harrison JBJ, Bras RL, Istanbuloglu E. 2013. On the observed ecohydrologic dynamics of a semiarid basin with aspect-delimited ecosystems. *Water Resources Research* **49**: 8263–8284. DOI:10.1002/2013WR014364.
- Heimsath AM, Dietrich WE, Nishiizumi K, Finkel RC. 1997. The soil production function and landscape equilibrium. *Nature* **388**: 358–361. DOI:10.1038/41056.
- Holbrook WS, Riebe CS, Elwaseif M, Hayes JL, Basler-Reeder K, Harry DL, Malazian A, Dosseto A, Hartsough PC, Hopmans JW. 2014. Geophysical constraints on deep weathering and water storage potential in the southern Sierra Critical Zone Observatory. *Earth Surface Processes and Landforms* **39**: 366–380. DOI:10.1002/esp.3502.
- Istanbuloglu E, Yetemen O, Vivoni ER, Gutiérrez-Jurado HA, Bras RL. 2008. Eco-geomorphic implications of hillslope aspect: inferences from analysis of landscape morphology in central New Mexico. *Geophysical Research Letters* **35**. DOI:10.1029/2008GL034477.L14403.
- Iverson LR, Prasad AM, Rebbeck J. 2004. A comparison of the integrated moisture index and the topographic wetness index as related to two years of soil moisture monitoring in Zaleski State Forest, Ohio. http://www.fs.fed.us/ne/newtown_square/publications/technical_reports/pdfs/2004/316papers/iversonGTR316.pdf
- Lanni C, McDonnell J, Hopp L, Rigon R. 2013. Simulated effect of soil depth and bedrock topography on near-surface hydrologic response and slope stability. *Earth Surface Processes and Landforms* **38**: 146–159. DOI:10.1002/esp.3267.

- Lebedeva MI, Brantley SL. 2013. Exploring geochemical controls on weathering and erosion of convex hillslopes: beyond the empirical regolith production function. *Earth Surface Processes and Landforms* **38**: 1793–1807. DOI:10.1002/esp.3424.
- Lebedeva MI, Fletcher RC, Brantley SL. 2010. A mathematical model for steady-state regolith production at constant erosion rate. *Earth Surface Processes and Landforms* **35**: 508–524. DOI:10.1002/esp.1954.
- Liu J, Chen X, Lin H, Liu H, Song H. 2013. A simple geomorphic-based analytical model for predicting the spatial distribution of soil thickness in headwater hillslopes and catchments. *Water Resources Research* **49**: 7733–7746. DOI:10.1002/2013WR013834.
- Moore ID, Gessler PE, Nielsen GA, Peterson GA. 1993. Soil attribute prediction using terrain analysis. *Soil Science Society of America Journal* **57**: 443. DOI:10.2136/sssaj1993.03615995005700020026x.
- Muldavin E, Tonne P. 2003. *A Vegetation Survey and Preliminary Ecological Assessment of Valles Caldera National Preserve, New Mexico*, Report for Cooperative Agreement. University of New Mexico: Albuquerque, NM.
- Naylor S, Gabet EJ. 2007. Valley asymmetry and glacial versus nonglacial erosion in the Bitterroot Range, Montana, USA. *Geology* **35**: 375–378. DOI:10.1130/G23283A.1.
- Nicótina L, Tarboton DG, Tesfa TK, Rinaldo A. 2011. Hydrologic controls on equilibrium soil depths. *Water Resources Research* **47**. DOI:10.1029/2010WR009538.W04517
- Pavich MJ, Leo GW, Obermeier SF, Estabrook JR. 1989. *Investigations of the characteristics, origin, and residence time of the upland residual mantle of the Piedmont of Fairfax County, Virginia*, US Geological Survey Professional Paper 1352. US Geological Survey: Reston, VA.
- Pelletier JD, McGuire LA, Ash JL, Engelder TM, Hill LE, Leroy KW, Orem CA, Rosenthal WS, Trees MA, Rasmussen C, Chorover J. 2011. Calibration and testing of upland hillslope evolution models in a dated landscape: Banco Bonito, New Mexico. *Journal of Geophysical Research: Earth Surface* **116**. DOI:10.1029/2011JF001976. F04004
- Pelletier JD, Rasmussen C. 2009. Geomorphically based predictive mapping of soil thickness in upland watersheds. *Water Resources Research* **45**. DOI:10.1029/2008WR007319.W09417
- Phillips EH, Goff F, Kyle PR, McIntosh WC, Dunbar NW, Gardner JN. 2007. The $^{40}\text{Ar}/^{39}\text{Ar}$ age constraints on the duration of resurgence at the Valles Caldera, New Mexico. *Journal of Geophysical Research: Solid Earth* **112**. DOI:10.1029/2006JB004511.B08201
- Pierce KL, Colman SM. 1986. Effect of height and orientation (microclimate) on geomorphic degradation rates and processes, late-glacial terrace scarps in central Idaho. *Geological Society of America Bulletin* **97**: 869–885. DOI:10.1130/0016-7606(1986).
- Poulos MJ, Pierce JL, Flores AN, Benner SG. 2012. Hillslope asymmetry maps reveal widespread, multi-scale organization. *Geophysical Research Letters* **39**. DOI:10.1029/2012GL051283.L06406
- Rempe DM, Dietrich WE. 2014. A bottom-up control on fresh-bedrock topography under landscapes. *Proceedings of the National Academy of Sciences* **111**: 6576–6581. DOI:10.1073/pnas.1404763111.
- St Clair JS, Moon S, Holbrook WS, Perron JT, Riebe CS, Martel SJ, Carr B, Harman C, Singha K, Richter D de B. 2015. Geophysical imaging reveals topographic stress control of bedrock weathering. *Science* **350**: 534–538. DOI:10.1126/science.aab2210.
- Slim M, Perron JT, Martel SJ, Singha K. 2014. Topographic stress and rock fracture: a two-dimensional numerical model for arbitrary topography and preliminary comparison with borehole observations. *Earth Surface Processes and Landforms* **40**(4): 512–529. DOI:10.1002/esp.3646.
- Soil Survey Staff. 1999. *Soil Taxonomy: A Basic System of Soil Classification for Making and Interpreting Soil Surveys*. In US Department of Agriculture Handbook 436, Second edn. Natural Resources Conservation Service: Washington, DC.
- Tarboton DG. 1997. A new method for the determination of flow directions and upslope areas in grid digital elevation models. *Water Resources Research* **33**: 309–319. DOI:10.1029/96WR03137.
- Tesfa TK, Tarboton DG, Chandler DG, McNamara JP. 2009. Modeling soil depth from topographic and land cover attributes. *Water Resources Research* **45**. DOI:10.1029/2008WR007474.W10438
- West N, Kirby E, Bierman P, Clarke BA. 2014. Aspect-dependent variations in regolith creep revealed by meteoric ^{10}Be . *Geology* **42**: 507–510. DOI:10.1130/G35357.1.
- Zapata-Rios X, Brooks PD, Troch PA, McIntosh J, Guo Q. 2015. Influence of terrain aspect on water partitioning, vegetation structure and vegetation greening in high-elevation catchments in northern New Mexico. *Ecohydrology*. DOI:10.1002/eco.1674.